Anharmonic phonon self-energy and anomalous thermal transport in the quaternary compound $BaAg_2SnSe_4$

Qing-Yu Xie,[1,2] Feng Xiao,[2,3] Kai-Wang Zhang,[1,*] and Bao-Tian Wang[2,3,4,†]
[1]*School of Physics and Optoelectronics, Xiangtan University, Xiangtan 411105, China*
[2]*Institute of High Energy Physics, Chinese Academy of Science, Beijing 100049, China*
[3]*Spallation Neutron Source Science Center, Dongguan 523803, China*
[4]*Collaborative Innovation Center of Extreme Optics, Shanxi University, Taiyuan 030006, China*

(Received 30 April 2024; revised 17 June 2024; accepted 26 June 2024; published 9 July 2024)

Accurate prediction of thermal transport properties and fundamental understanding of multiphonon interaction in strong anharmonic systems are nontrivial but challenging in condensed matter physics and materials science. Herein, we investigate the anharmonic phonon self-energy, lattice dynamic, and thermal transport in quaternary compound $BaAg_2SnSe_4$ using the self-consistent phonon (SCP) theory and the Wigner thermal transport model. At each temperature (T), we utilize the SCP method, which includes the bubble and loop diagrams, to calculate anharmonic phonon frequencies and obtain particle-like phonon propagate and wavelike phonon coherent thermal conductivity within the framework of the Peierls-Boltzmann transport equation. Results show that (i) the rattling-like vibrations of the disordered Ag-Ag dimers result in anharmonic non-Lorentzian–shape phonon energy power spectral for some low-energy phonons and thus these phonon modes are overdamped; (ii) anharmonic hardening effect suppresses the low-frequency phonon scattering strength via diminishing scattering phase space, offsetting the phonon population effect as T increases; and (iii) strong phonon broadening leads to non-negligible coherent contribution, which contributes up to 35.7% of the total lattice thermal conductivity (κ_L) at 800 K, indicating partial breakdown of the conventional phonon gas model. Taking into account the phonon anharmonic renormalization and the two-channel phonon thermal transport can effectively resolve the discrepancy between theoretical and experimental values of κ_L and yield a better description, both in magnitude and T dependence. Our work demonstrates the effect of phonon broadening and frequency shift induced by multiphonon interaction on κ_L and deepens the understanding of thermal transport in disordered crystals with strong anharmonicity.

DOI: 10.1103/PhysRevB.110.045203

I. INTRODUCTION

Materials with ultralow κ_L have been extensively applied in practical applications, e.g., high-performance thermoelectrics, thermal barrier coatings, and photovoltaics [1,2]. Fundamental understanding of phonon dynamics and thermal transport mechanisms in crystalline compounds with intrinsic low κ_L is physically interesting and technically important. Such kind of investigation can reveal the intrinsic dynamics of the rattling atoms [3–5], static distortion [6], and bonding heterogeneity [7,8], which are tightly related to low κ_L. Phonon mean-free path (MFP) approaches the Ioffe-Regel limit and leads to the qualitative breakdown of the conventional description of the particle-like propagation of the phonon wave packets in typical crystals [9–13]. Previous studies broke the potential boundaries between traditional crystalline and amorphous glass through two-channel thermal transport model: both the propagating particle-like phonon wave packets and the localized phonon modes (locons) associated with the random walk (hopping) among the uncorrelated oscillators [13–17].

In the two-channel thermal transport model, some phonon modes having MFP shorter than the Ioffe-Regel limit cannot be regarded as the normal phonon modes, which contribute to the thermal transport as conventional phonon gas. These modes are diffuson-like phonons that obey the diffusion thermal transport theory [10,12,13,18]. The thermal transport contribution of the diffusion-like phonon channel can be evaluated by the Einstein or Cahill-Watson-Pohl formula [18]. In the Einstein model, each atom can be regarded as an independent quantum harmonic oscillator with the same frequency. Einstein assumed that the contribution of diffusion phonons to the thermal transport arises from the random walk of the heat from random phases between neighboring atoms and thus is independent of the phonon lifetime and frequency [18]. Further, Cahill *et al.* introduced the varying frequency associated with sound speed in crystal to correct the Einstein model. Each atom interacts with its neighbors through harmonic force on a simple cubic lattice and the lifetime of each oscillator is assumed to be one-half of the period of the vibration [18]. The two-channel heat-transport model effectively resolves the discrepancy between experimental and theoretical and enriches the understanding of the microscopic mechanism of thermal transport, allowing us to revisit the phonon dynamics [10,13]. Despite tremendous efforts, the comprehensive understanding

*Contact author: kwzhang@xtu.edu.cn
†Contact author: wangbt@ihep.ac.cn

of the microscopic mechanism of phonon dynamics in simple crystals with κ_L approaching the amorphous limit remains a great challenge [18–21].

However, there remain some open questions in the two-channel thermal transport model. Particularly, how do the normal phonons interact with diffuson-like phonons [10,22–25]? On the other hand, some infrared and Raman spectral experimental studies show that many zone-center optical phonons still possess short or nearly zero MFP, suggesting that the phonon remains well defined, with precise frequencies and linewidths [26,27]. Experimental Raman spectra, specific heat, and T dependence of $\kappa_L(T)$ still support the characteristics of phonons in typical crystalline compounds [13,23]. Moreover, the failure of the conventional Peierls-Boltzmann transport equation (PBTE) is it does not capture the phonon wave effects in superlattices or phononic crystals [28,29]. Meanwhile, lattice anharmonicity can induce multiphonon interaction, which leads to the phonon frequencies shift and the phonon states broadening [30–34]. Thus, it is of great significance to revisit the impact of the high-order anharmonicity as well as the phonon wave tunneling on the phonon transport [22–25,35].

Copper- or silver-based thermoelectric materials exhibit abundant anharmonic phonon dynamics and atomic dynamics due to the loose bonding connected with Cu or Ag atoms, e.g., strong bonding heterogeneity [7,36] and rattling dynamics [4,37]. These materials possess partial liquidlike lattice, resulting in the qualitative suppression of the transverse phonon mode propagation, e.g., Cu_3SbSe_3 [38,39], $AgCrSe_2$ [40–43], and $Cu_2Se_{1-s}S_x$ [44,45]. In addition, the soft bonding of Ag atoms induces local structural distortions and leads to a strong crystallographic inhomogeneity in $AgPbBiSe_3$ [36]. The large atomic mean-square displacement and the rattling-like vibrations result in the pronounced avoided crossing between acoustic and low-lying optical phonon modes [4], leading to decreases of the acoustic phonon lifetime and phonon group velocities and also reduced κ_L, e.g., $CsAg_5Te_3$ [46], MgAgSb [6], and $CsCu_4Se_3$ [47]. These have provided substantial research resources for studying the phonon dynamics of strong anharmonic lattice.

Quaternary compound $BaAg_2SnSe_4$ has attracted widespread attention due to its ultralow κ_L and high thermoelectric performance [48–51]. Previous studies ascribed the microscopic mechanism of the ultralow κ_L to the rattling vibrations of the Ag atoms softening lattice, low specific heat, and low phonon group velocities [48,50]. However, the calculated values severely underestimated the experimental values and such differences were attributed to the experimental polycrystalline sample and the hot-press method [48], despite the fact that additional nonintrinsic grain-boundary scattering in polycrystalline samples could further reduce the κ_L. The underlying physical microscopic mechanisms of the ultralow κ_L and its weak T dependence, which deviates far from the T^{-1} behavior in conventional phonon gas, deserve further comprehensive investigation. Recent study by Chang *et al.* [52] has resolved this discrepancy through combining the two-channel thermal transport model and temperature-dependent effective potential method to some extent; they highlight the importance of temperature-dependent interaction force constants and wavelike tunneling phonons. However, the underlying physical mechanism of high-order anharmonic coupling with harmonic vibration eigenvectors thereby inducing phonon frequency shifts remains elusive. Meanwhile, the physical mechanism of anharmonic hardening effect on particle-like phonon thermal transport lacks a distinct physical picture. Furthermore, the atomic-level understanding of the anisotropic heat-transport behavior of both particle-like propagation of phonon wave packets and wavelike tunneling phonons remains stuck on phenomenological stage.

In this paper, using self-consistent phonon (SCP) theory and the Wigner thermal transport model, we investigate the phonon dynamics in the quaternary compound $BaAg_2SnSe_4$. The ultralow κ_L of this Ag-based material can be attributed to the rattling-like vibrations of the highly disordered Ag-Ag dimers, which result in low-energy phonons overdamped and hinder the thermal conduction propagation. The coexistence of the anharmonic hardening effect as well as the non-negligible coherent thermal contribution leads to the weak dependence of κ_L on T, which strongly deviates from the conventional phonon gas model. These results deepen the understanding of the phonon dynamics in strong anharmonic system and provides a valuable reference to push low κ_L to its limit.

II. COMPUTATION DETAILS

A. Density-functional theory calculations

In this paper, the projector augmented wave (PAW) potentials [53,54] are employed to treat the Ba ($5s^2\,5p^6\,6s^2$), Ag ($5s^1\,4d^{10}$), Sn ($5s^2\,5p^4$), Se ($4s^2\,4p^2$) shells as valence states as implemented in the Vienna *Ab initio* Simulation Package (VASP) code [55]. The Perdew-Burke-Ernzerhof functional revised for solids of the generalized gradient approximation is used for the exchange-correlation energy functional. Sufficient structural relaxation is performed on a $6 \times 6 \times 6$ Monkhorst-Pack k-point grid with a plane-wave energy cutoff of 500 eV. The total energy difference is converged to within 10^{-8} eV/Å and a tight convergence criterion of 10^{-4} eV/Å is set for the Hellman-Feynman force acting on each atom. The optimized lattice constants (a, b, c) of $BaAg_2SnSe_4$ compound, which crystallizes in orthorhombic structure with space group $I222$ (No.23), are (7.151, 7.711, 8.589) Å, respectively, and are in good agreement with previous experimental values of (7.116, 7.499, 8.337) Å [51] and (7.074, 7.454, 8.289) Å [49], as well as theoretical values of (7.149, 7.712, 8.589) Å [48] and (7.141, 7.713, 8.582) Å [50] within the acceptable error (<3%).

B. Anharmonic force constants

We obtain the harmonic interatomic force constants (IFCs) using the finite-displacement approach using a $2 \times 2 \times 2$ supercell containing 128 atoms as implemented in the PHONOPY package [56]. For the cubic and quartic IFCs, we utilize the compressive-sensing lattice dynamics (CSLD) method, which finds sparse solutions from the force-displacement datasets through advanced compressive-sensing techniques [35,57,58]. Herein, instead of conventional *ab initio* molecular dynamics simulations sampling, we adopt a stochastic scheme

which iteratively generates superimposing harmonic phonon eigenmodes with random amplitudes and phase factors at 50 K as performed in the HIPHIVE package and our in-house code [59,60]. Then, we perform highly accurate density-functional theory self-consistent calculations for selected 160 configurations with a $3 \times 3 \times 3$ k mesh and a tight criterion of convergence for total energy of 10^{-8} eV to obtain high-quality force-displacement datasets. Finally, we fit anharmonic IFCs (cubic and quartic terms), which include up to the tenth (11 bohr) and the seventh (9 bohr) nearest-neighbors' interatomic interactions, respectively, by the least absolute shrinkage and the selection operator technique [61,62] with a relative error of 1.61% [see Figs. S1 and S2 in the Supplemental Material (SM)] [63].

C. Self-consistent phonon calculations

To obtain anharmonic renormalization phonon dispersion curves at finite T, we employ the SCP theory, which considers only the first-order correction from the quartic anharmonicity, i.e., the loop diagram. In this scheme, the anharmonically renormalized phonon energy is determined from the pole of the many-body Green's function [31,64]. The resultant SCP equation which neglects the nondiagonal terms can be represented as

$$\Omega_{\mathbf{q}}^2 = \omega_{\mathbf{q}}^2 + 2\Omega_{\mathbf{q}} I_{\mathbf{q}}, \tag{1}$$

where $\omega_{\mathbf{q}}$ is the harmonic frequency and $\Omega_{\mathbf{q}}$ is the renormalized phonon frequency at finite T. The quantity $I_{\mathbf{q}}$ is defined as

$$I_{\mathbf{q}} = \frac{1}{2}\sum_{\mathbf{q}'} \frac{\hbar\Phi(\mathbf{q}:-\mathbf{q}:\mathbf{q}':-\mathbf{q}')}{4\Omega_{\mathbf{q}}\Omega_{\mathbf{q}'}}[1+2n(\Omega_{\mathbf{q}'})], \tag{2}$$

where N, $\hbar$, n, and Φ are, respectively, the number of the sampled wave vectors, the reduced Planck constant, the phonon population, and the reciprocal representation of the quartic IFCs. In the SCP scheme, T affects the phonon population that obeys the Bose-Einstein statistics.

To avoid overestimation of the phonon-energy hardening, the second-order SCP calculations which consider the bubble diagrams ascribing from the cubic IFCs are performed within the quasiparticle approximation as Tadano suggested [34]. This amendment generally induces a negative shift of the phonon energy and can be evaluated as the following self-consistent equation:

$$\Omega_{\mathbf{q},B}^2 = \Omega_{\mathbf{q}}^2 - 2\Omega_{\mathbf{q}}^2 \mathrm{Re}\sum\nolimits_{\mathbf{q}}^{(B)}(\Omega_{\mathbf{q}}), \tag{3}$$

$$\Sigma_q^{(\mathrm{B})}(\Omega\mathbf{q}) = \frac{1}{16}\sum_{q',q''} \frac{\hbar|\Phi_3(-q;q';q'')|^2}{\omega_q\omega_{q'}\omega_{q''}} \times \Delta(-\mathbf{q}+\mathbf{q}_1+\mathbf{q}_2) f(1,2,\omega+i\grave{o}), \tag{4}$$

$$f(1,2,\omega+i\grave{o}) = \sum_{\sigma=-1,1}\sigma\left[\frac{1+n(\omega_{\mathbf{q}'})+n(\omega_{\mathbf{q}''})}{\omega+i\grave{o}+\sigma(\omega_{\mathbf{q}'}+\omega_{\mathbf{q}''})} - \frac{n(\omega_{\mathbf{q}'})-n(\omega_{\mathbf{q}''})}{\omega+i\grave{o}+\sigma(\omega_{\mathbf{q}'}-\omega_{\mathbf{q}''})}\right], \tag{5}$$

where $\sum_{\mathbf{q}}^{(\mathrm{B})}(\Omega_{\mathbf{q}})$ represents the phonon bubble self-energy at finite T, Φ_3 is the cubic IFCs, and B denotes the bubble diagram. In this paper, the self-consistent iterative solving of the SCP is performed in the ALAMODE package.

D. Phonon thermal transport

The contribution to the thermal conductivity from the particle-like propagation phonon under the single-mode relaxation-time approximation (SMRTA) is [65]

$$\kappa_{\mathrm{p}} = \frac{1}{VN}\sum_{\mathbf{q}} C_{\mathbf{q}}(T)\upsilon_{\mathbf{q}}(T)\upsilon_{\mathbf{q}}(T)\tau_{\mathbf{q}}(T), \tag{6}$$

where $C_{\mathbf{q}}$, $\upsilon_{\mathbf{q}} = d\Omega\mathbf{q}/d\mathbf{q}$, and $\tau_{\mathbf{q}} = 1/[2\Gamma_{\mathbf{q}}(\Omega_{\mathbf{q}})]$ are mode heat capacity, phonon group velocities, and phonon relaxation time, respectively. The phonon linewidth $\Gamma\mathbf{q}(\Omega\mathbf{q})$ can be calculated from the imaginary part of the phonon self-energy $\Sigma\mathbf{q}(\Omega\mathbf{q})$ of the bubble diagram as

$$\Gamma_{\mathbf{q}}(\Omega\mathbf{q}) = \frac{\pi}{2N}\sum_{\mathbf{q}',\mathbf{q}''} \frac{\hbar|\Phi(-\mathbf{q},\mathbf{q}',\mathbf{q}'')|^2}{8\Omega_{\mathbf{q}}\Omega_{\mathbf{q}'}\Omega_{\mathbf{q}''}}[(n_{\mathbf{q}'}+n_{\mathbf{q}''}+1) \times \delta(\omega-\Omega_{\mathbf{q}'}-\Omega_{\mathbf{q}''}) - 2(n_{\mathbf{q}'}-n_{\mathbf{q}''}) \times \delta(\omega-\Omega_{\mathbf{q}'}+\Omega_{\mathbf{q}''})], \tag{7}$$

and the real part of the bubble diagram can be written as

$$\Delta\mathbf{q}(\omega) = \frac{18\pi}{\hbar^2}\sum_{\mathbf{q}'\mathbf{q}''}|\Phi_{-\Omega\mathbf{q}\Omega\mathbf{q}'\Omega\mathbf{q}''}|^2 \times \left\{\left[\frac{(n_{\mathbf{q}'}+n_{\mathbf{q}''}+1)}{(\Omega-\Omega_{\mathbf{q}'}-\Omega_{\mathbf{q}''})_{\mathrm{p}}} - \frac{(n_{\mathbf{q}'}+n_{\mathbf{q}''}+1)}{(\Omega+\Omega_{\mathbf{q}'}+\Omega_{\mathbf{q}''})_{\mathrm{p}}}\right] + \left[\frac{(n_{\mathbf{q}'}-n_{\mathbf{q}''})}{(\Omega+\Omega_{\mathbf{q}'}-\Omega_{\mathbf{q}''})_{\mathrm{p}}} - \frac{(n_{\mathbf{q}'}-n_{\mathbf{q}''})}{(\Omega-\Omega_{\mathbf{q}'}+\Omega_{\mathbf{q}''})_{\mathrm{p}}}\right]\right\} \tag{8}$$

The phonon spectral function of the bubble diagram for single-phonon mode is [40,66,67]

$$S_{\mathbf{q},s}(\Omega) = \frac{2\Omega_{\mathbf{q},s}\Gamma_{\mathbf{q},s}(\Omega)}{\left[\Omega^2-\Omega_{\mathbf{q},s}^2-2\Omega_{\mathbf{q},s}\Delta_{\mathbf{q},s}(\Omega)\right]^2+4\Omega_{\mathbf{q},s}^2\Gamma_{\mathbf{q},s}^2(\Omega)}, \tag{9}$$

where $\Omega_{\mathbf{q},s}$ is the eigenfrequency of phonon ($\mathbf{q}$, s) with the wave vector $\mathbf{q}$ and polarization index s. In the conventional PBTE physical picture, the phonon quasiparticle approximation is valid only when linewidths of phonons are less than the interbranch spacings. However, it cannot capture and describe the thermal transport behavior of the strong phonon broadening in severely anharmonic systems because of the loss of coherence component, i.e., the off-diagonal terms of the heat-flux operators. The Wigner thermal transport model within the SMRTA is represented as [20,22,25]

$$\kappa_{p/c} = \frac{\hbar^2}{k_B T^2 V N_0}\sum_{\mathbf{q}}\sum_{j,j'}\frac{\Omega_{\mathbf{q}j}+\Omega_{\mathbf{q}j'}}{2}\upsilon_{\mathbf{q}jj'}\otimes\upsilon_{\mathbf{q}j'j} \times \frac{\Omega_{\mathbf{q}j}n_{\mathbf{q}j}(n_{\mathbf{q}j}+1)+\Omega_{\mathbf{q}j'}n_{\mathbf{q}j'}(n_{\mathbf{q}j'}+1)}{4(\Omega_{\mathbf{q}j}-\Omega_{\mathbf{q}j'})2+(\Gamma_{\mathbf{q}j}+\Gamma_{\mathbf{q}j'})2}(\Gamma_{\mathbf{q}j}+\Gamma_{\mathbf{q}j'}), \tag{10}$$

$$\upsilon_{\mathbf{q}jj'} = \frac{\langle e_{\mathbf{q}j}|\frac{\partial D(\mathbf{q})}{\partial\mathbf{q}}|e_{\mathbf{q}j'}\rangle}{2\sqrt{\Omega_{\mathbf{q}j}\Omega_{\mathbf{q}j'}}}, \tag{11}$$

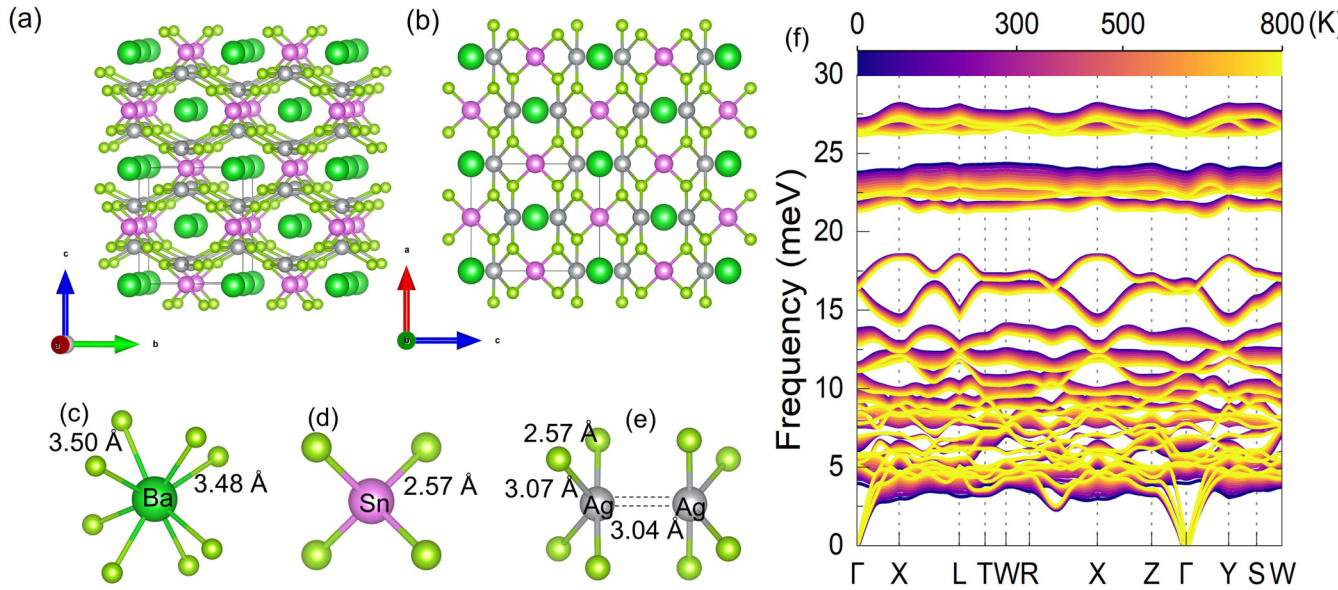

FIG. 1. (a), (b) Crystal structure of $BaAg_2SnSe_4$, where the dark-green, green, pink, and gray balls represent Ba, Se, Sn, and Ag atoms, respectively. (c)–(e) Local coordinations of the [BaSe8] polyhedra, [SnSe4] tetrahedral, and two distorted [AgSe4] tetrahedra consist of Ag-Ag dimers. (f) Anharmonically renormalized phonon dispersions of $BaAg_2SnSe_4$ at finite T (0–800 K).

where subscripts p and c represent particle-like propagation of phonon wave packets and wavelike phonon tunneling of heat carrying, and $\upsilon_{\mathbf{q}jj'}$ is the interband generalization of the group velocity [20]. Notably, when the second summation in Eq. (10) is performed over the diagonal terms, i.e., $j = j'$, it reduces to the PBTE equation in the conventional phonon gas model. The total κ_L is given as $\kappa_L = \kappa_p + \kappa_c$. In this paper, the q mesh for calculating the particle-like phonon thermal conductivity in the PBTE framework is set as $20 \times 20 \times 20$, which gives well-converged results as implemented in the ALAMODE package (see Fig. S3 in the SM) [63]. More computation details can be seen in workflows of Figs. S4 and S5 in the SM [63].

III. RESULTS AND DISCUSSION

A. Structure and phonon anharmonicity

The crystal structure of $BaAg_2SnSe_4$ is shown in Fig. 1. In this orthorhombic structure, each Sn or Ag atom is surrounded by four Se atoms, forming [SnSe4] tetrahedra and [AgSe4] tetrahedra [51]. The [AgSe4] exhibits strong distorted tetrahedra with a large discrepancy between short (2.57 Å) and long (3.07 Å) Ag–Se bond length and the maximum Se–Ag–Se bond angle is as large as 179.1° [47]. The nearest-neighbors' two distorted and edge-sharing [AgSe4] tetrahedra are linked weakly by the Ag-Ag dimers, which lie along the c-axis direction [50]. The [SnSe4] tetrahedra and [AgSe4] tetrahedra are linked through their sharing Se atoms to form a three-dimensional network that confines distorted hexagonal-shaped tunnels with diameters about 7.7 and 5.5 Å along the b and c axes, respectively. In each tunnel, one Ba^{2+} cation is accommodated and has relatively large distances to its neighbor Se atoms. As indicated in Fig. 1(a), the special tunnel can be viewed clearly along the b axis. From a structural perspective, such a tunnel network provides sufficient vibrational space for the highly disordered Ag-Ag dimers and may be associated with the rattling dynamic, disorder dynamic, and local dynamics, which may disrupt the thermal transport. The highly disordered [AgSe4] tetrahedra as well as the weakly bonded Ag-Ag dimers are expected to lead to nearly nondispersive low-lying optical phonon mode and thus result in ultralow κ_L.

Taking into account the cubic and quartic anharmonicity, we calculate the phonon dispersions at finite T from 0 to 800 K and plot the results in Fig. 1(f). As shown, there exist numerous quasilocalized low-lying optical modes in the low-frequency region around 3–8 meV, offering multiple scattering channels and thus effectively scattering the heat-carrying phonons [68,69]. These nearly nondispersive optical phonon modes can be attributed to the rattling vibrations of the Ag cation and the weakly bonded Ag-Ag dimers according to the element-resolved phonon density of states (PhDOSs), as shown in Fig. S6 in the SM [63]. Meanwhile, the rattling mode associated with the guest Ag cations can increase the linewidth of the acoustic phonon modes and reduce the phonon group velocities This feature is a common physical characteristic in the guest-host system [33] or cagelike system [4]. Furthermore, the transverse optical mode (TO) couples with the longitudinal acoustic phonon mode (LA), leading to optical-acoustic phonon polarization hybridization. This hybridization behavior induces the optical phonon eigenvectors into acoustic phonons, resulting in an increased phonon scattering rate according to anharmonicity theory [70,71].

Upon heating, phonon modes in the low-frequency region (up to 8 meV) display significant hardening behavior, especially for the rattling modes which are mainly dominated by the Ag atoms' rattling vibrations. These modes exhibit evident T-dependent features, as revealed by the element-decomposed PhDOSs in Fig. S6 in the SM [63]. On the contrary, the phonons above 8 meV show softening characteristics upon heating. Here, the phonons are mainly associated with the [SnSe4] tetrahedron. Besides, as shown in Fig. S7 in the SM

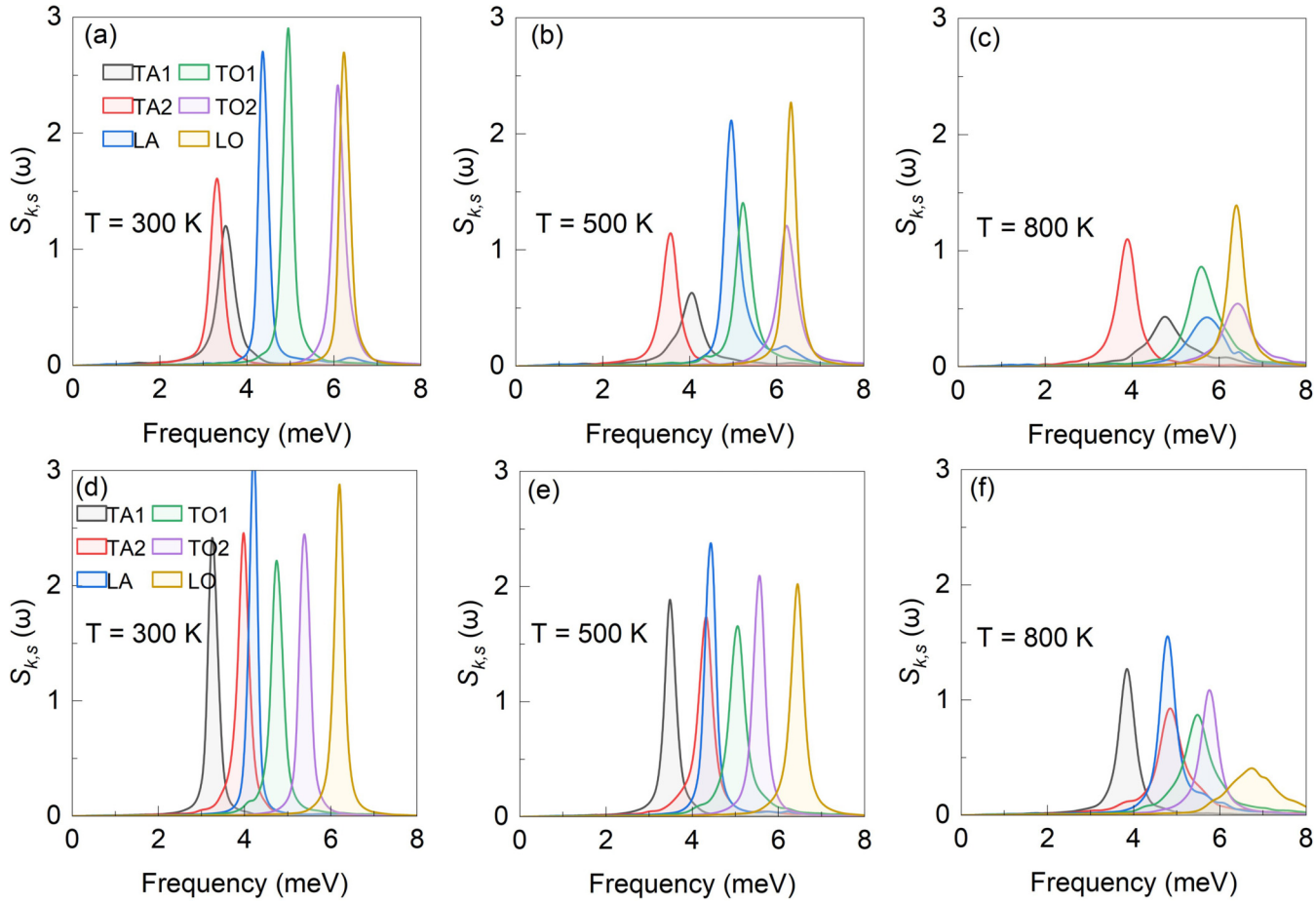

FIG. 2. (a)–(c) Phonon spectral function $S_{\mathbf{q},s}(\omega)$ at X point at 300, 500, and 800 K in the Brillouin zone. (d)–(f) $S_{\mathbf{q},s}(\omega)$ at W point at 300, 500, and 800 K in the Brillouin zone. The black, red, blue, green, purple, and yellow solid lines represent the transverse acoustic (TA1, TA2), longitudinal acoustic (LA), transverse optical (TO1, TO2) phonon modes, and longitudinal optical (LO) phonon modes, respectively. Phonon linewidth broadening and frequency shift due to T-induced anharmonic renormalization are evident.

[63], the average mean-square displacement (MSD) of Ag atoms is significantly larger than those of other atoms, further verifying its loose bonding strength. Interestingly, taking into account the quartic anharmonicity, the MSD of all atoms is significantly suppressed when compared with those by the harmonic approximation. However, the cubic anharmonicity softens the phonon frequency (see Fig. S8), thereby inducing a qualitative increase in MSD. Physically, the dominate and positive quartic anharmonicity coefficient induces a deeper and flatter potential energy surface (PES) of the dynamic eigenvectors than that of harmonic approximation. However, involving cubic anharmonicity, PES becomes shallower and yields an increased MSD.

B. Anharmonic lattice dynamics

Phonon spectral function $[S_{\mathbf{q},s}(\omega)]$ can directly reflect anharmonic lattice dynamics physically [40,66]. Fundamentally, anharmonicity induces the multiphonon interactions and renormalizes the energy spectral of the phonon quasiparticles. Both of them give rise to phonon frequency shifts (shifting the peak positions in phonon energy spectral) and introduce finite phonon broadening (phonon damping or the full width at half maximum) in solids [72–76]. Here, we present $S_{\mathbf{q},s}(\omega)$ in full frequency dependence on the self-energy of the transverse acoustic (TA1, TA2) and optical (TO1, TO2) phonon modes and longitudinal acoustic (LA) and optical (LO) phonon modes at X and W points in the Brillouin zone in Fig. 2. Apparently, the calculated $S_{\mathbf{q},s}(\omega)$ exhibits significant hardening behavior, e.g., the peak position of the LA phonon mode at X point appearing as a blueshift on heating. Meanwhile, the $S_{\mathbf{q},s}(\omega)$ of all the phonon modes are weakened, broadened, and diffused as T increases, indicating significant anharmonic renormalization and enhanced phonon linewidth (scattering rate). Physically, this anharmonic feature is required and constrained by the normalization of the $S_{\mathbf{q},s}(\omega)$, i.e., $\int_0^\infty \frac{d\omega}{2\pi} S_k(\omega) = 1$. Further, the $S_k(\omega)$ of the LA phonon mode shows a double-peak structure. A broad shoulder appears in the optical phonon zone, especially under high T. This feature significantly deviates from the Lorentzian behavior of other phonon modes. The non-Lorentzian shape of $S_k(\omega)$ for the LA mode is the consequence of the coupling between all phonon modes in the Brillouin zone, rather than interacting with specific phonons. Such an anomalous non-Lorentzian peak shape was also found in other famous severely anharmonic materials, e.g., PbTe [75], SnSe [72], CuCl [77,78], and

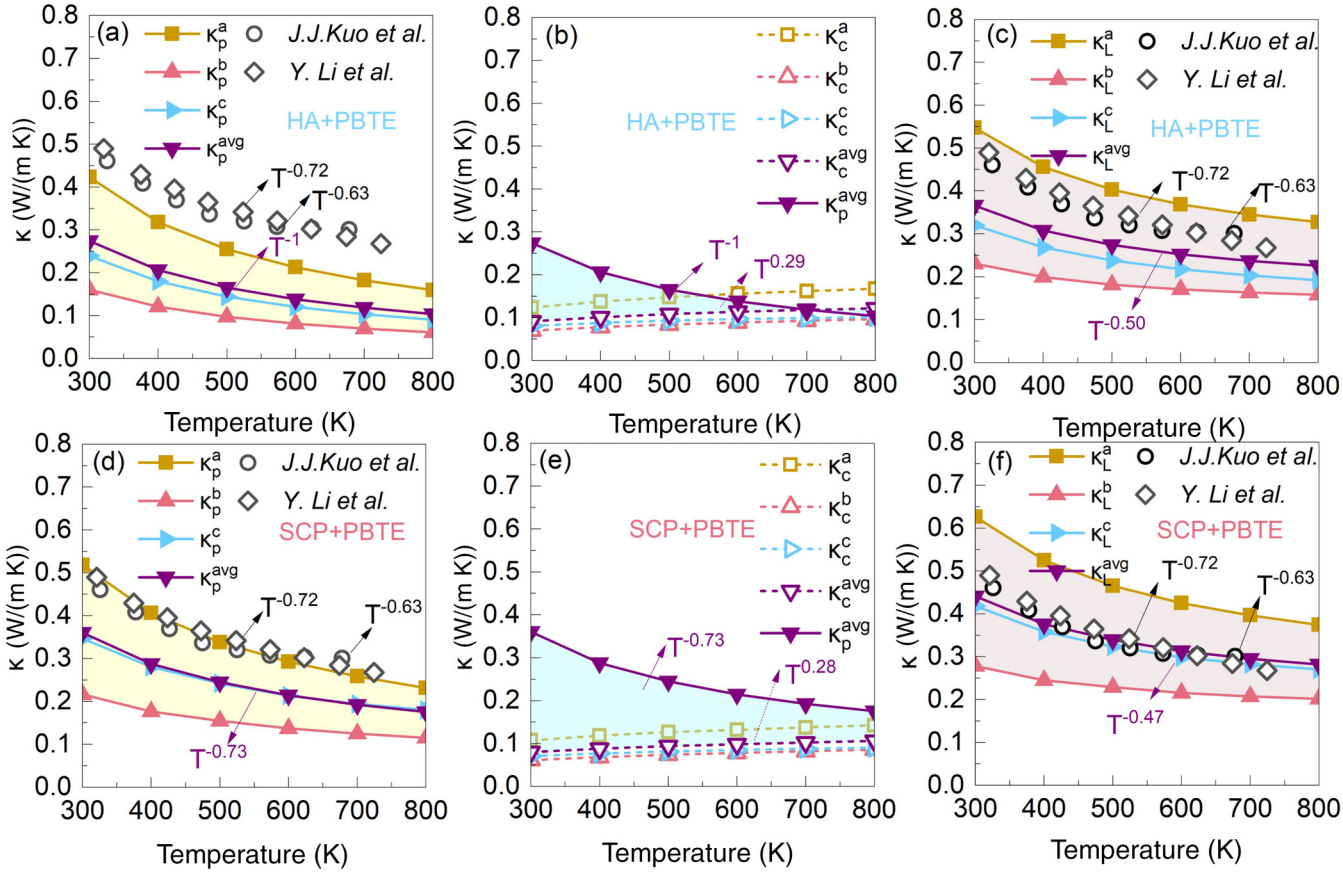

FIG. 3. The calculated thermal conductivity arising from particle-like propagation of phonons and wavelike tunneling phonons. (a), (d) particle-like phonons contribution to $\kappa_{\rm L}$, (b), (e) wavelike phonons contribution to $\kappa_{\rm L}$, (c), (f) the total $\kappa_{\rm L}$ in quaternary compound $BaAg_2SnSe_4$ within the work frame of HA/SCP + PBTE. The superscript *a/b/c* represents the Cartesian directions and the subscripts *p*, *c*, and L are propagating particle-like phonon wave packets, wavelike phonon tunneling of heat carrying, and $\kappa_{\rm L}$, respectively. $\kappa_{\rm L}^{\rm avg}$ represents the average of the calculated $\kappa_{\rm L}$ along three Cartesian directions, i.e., $\kappa_{\rm L}^{\rm avg} = (\kappa_p^a + \kappa_p^b + \kappa_p^c)/3$ at HA/SCP levels of thermal transport theory. The experimentally measured values are taken from Refs. [49,51].

$AgCrSe_2$ [40]. This anharmonic feature instead of the usual damped harmonic oscillator profile becomes more remarkable with increasing *T*. Interestingly, upon heating, the $S_{\mathbf{q},s}(\omega)$ of some phonon modes exhibit a transition from the Lorentzian peak to strongly anharmonic non-Lorentzian shape, e.g., the TA1 phonon mode at *X* point, the TO phonon mode at *W* points, and the TA2 phonon mode at *W* point. These modes with anomalous complex spectral line shapes are those that show the largest linewidth in the Lorentzian limit and can easily scatter with other phonon modes close in energy and acoustic modes close to Γ point.

C. Lattice thermal conductivity

Next, we perform a comprehensive analysis of the theoretical lattice thermal conductivities obtained by solving the PBTE within different levels of thermal transport theory, including both the conventional harmonic approximation (HA) and the anharmonically renormalized phonon frequencies at finite *T* obtained using the SCP method, namely, HA+PBTE and SCP+PBTE, respectively. We refer to the subsequent results as κ_p^{abc}(HA), $\kappa_{\rm c}^{abc}$ (HA), $\kappa_{\rm L}^{abc}$ (HA), κ_p^{abc}(SCP), $\kappa_{\rm c}^{abc}$ (SCP), and $\kappa_{\rm L}^{abc}$ (SCP), where superscript *a/b/c* represents Cartesian direction and subscripts *p*, *c*, and L are the propagating particle-like phonon wave packets, wavelike phonon tunneling of heat carrying, and $\kappa_{\rm L}$, respectively. As shown in Fig. 3(a), all the κ p(HA) results along the three Cartesian directions seriously underestimate the available experimental measured values [49,51], consistent with previous studies [48,50]. Meanwhile, the weak *T* dependence of the experimentally measured $\kappa_{\rm L}$, which decays as $T^{-0.72}$ [51] or $T^{-0.63}$ [49], does not comply with the T^{-1} behavior in the conventional phonon gas model [21]. This anomalous thermal transport behavior of slow reduction of $\kappa_{\rm L}$ implies the breakdown of the conventional phonon gas model in severely anharmonic solids. Interestingly, the wavelike phonon tunneling thermal transport contributions, which arise from the coherent coupling between different vibrational eigenstates, show a positive *T* dependence and rise as $T^{0.29}$ [see Fig. 3(b)]. Taking the off-diagonal contributions of the heat-flux operator into account, the calculated $\kappa_{\rm L}^{\rm avg}$(HA) is significantly improved. For example, $\kappa_c^{\rm avg}$(HA) accounts for 24.6% of contributions to that of $\kappa_{\rm L}^{\rm avg}$(HA) values at 300 K. The proportion increases to 53.9% as *T* increases to 800 K [see Fig. 3(c)]. Although the discrepancy between theory and experiment has been greatly

improved by taking into account the contributions from the wavelike phonon tunneling, it still does not accurately reproduce the experimental results, both in magnitude and T dependence.

The discrepancy of κ_{L} from the HA+PBTE frame and experiment implies the presence of strong higher anharmonicity and the necessity of anharmonic rationalization of the harmonic phonon frequencies. Employing the SCP+PBTE frame, our calculated κ_p^{avg}(SCP) increases close to the experimental values and shows a significantly improved relation of the T dependence, varying as $T^{-0.73}$. However, the result still does not meet well with the experiment data. Taking into account the contributions from the wavelike phonon tunneling, i.e., obtaining $\kappa_{\mathrm{L}}^{\mathrm{avg}}$(SCP) by adding κ_p^{avg}(SCP) with κ_c^{avg}(SCP), the results are quite close to the experimental observations. At 300 K, κ_c^{avg}(SCP) accounts for 18.2% of contributions to the $\kappa_{\mathrm{L}}^{\mathrm{avg}}$(SCP). This proportion increases to 35.7% as T increases to 800 K [see Figs. 3(d)–3(f)]. Without considering the second-order correction of the bubble diagram to phonon energy, the phonon energy and calculated lattice thermal conductivity will be qualitatively overestimated (see Figs. S9 and S10 in the SM) [63]. Therefore, invoking both the wavelike phonon tunneling and the anharmonic renormalization, we reproduce accurate results of the κ_{L}, which agrees well with experiments both in magnitude and T dependence. In this work, although the experimental results are well reproduced, we do not consider the thermal expansion effect that may cause slight differences. We will further discuss it to some extent in the subsequent Discussion section, Sec. III E.

From Fig. 3, results show that the anisotropic feature of the κ_{L} is evident. The κ_{L} results along the a axis are always the largest while those along the b axis are always the smallest. The values along the c axis are almost close to the averaged values. Such anisotropic feature of the κ_{L} is tightly related to the structural characteristic of $BaAg_2SnSe_4$, where the distorted hexagonal-shaped tunnels consisting of Ag-Sn-Se are along the a axis. The large tunnels, with diameters of about 7.7 and 5.5 Å along the b- and c axes, respectively, greatly hinder the thermal transport. A similar anisotropic feature of thermal conductivity has also been reported in our previous study of tetragonal α-$CsCu_5Se_3$ [64], where special peanut-shaped tunnels exist and are vertical to its ab plane.

D. Phonon thermal properties

Illustrating the anomalous thermal transport behavior in quaternary $BaAg_2SnSe_4$, we turn to explore the underlying microscopic mechanisms. To reveal the microscopic mechanisms of the hardening effect induced by the phonon anharmonic renormalization, we plot the κ_{L} spectra of κ_p^{avg}(HA) and κ_p^{avg}(SCP) at finite T in Fig. 4(a). As shown, all the cumulative κ_p^{avg} change rapidly before a low frequency of 10 meV and reach a plateau above it. Thus, the main contributions to the κ_{L} are mainly originated from the acoustic and low-lying quasilocalized phonon modes. As T increases, the large peak of $\kappa_p(\omega)$ shows a blueshift from 3 to 4 meV, implying the strong anharmonic hardening effect.

According to the previous analysis of $S_{\mathbf{q},s}(\omega)$ in low-energy regions, $S_{\mathbf{q},s}(\omega)$ of all the acoustic- as well as the low-lying optical phonon modes become broader and more diffuse upon heating, suggesting the enhanced scattering rates. However, the phonon anharmonic hardening effect results in different phonon frequencies and eigenvectors at finite T. As Fig. 4(b) shows, the scattering rates are generally enhanced on heating, yet the phonon modes associated with the Ag-Ag dimers' rattling-like vibrations in the low-frequency region below 10 meV are surprisingly reduced. Meanwhile, the scattering rate of some phonon modes in the low-frequency region significantly exceeds the amorphous limit, indicating the qualitative breakdown of phonon quasiparticle physical picture and phonon overdamped, consistent with the previous analysis of $S_{\mathbf{q},s}(\omega)$. Next, we analyze the intrinsic effect of phonon group velocities in determining κ_p. As shown in Fig. 4(c), phonon group velocities of phonon modes in low-energy regions are weakly increased upon heating, whereas the high-energy phonon modes are decreased, in good agreement with our previous analysis of phonon dispersion curves at finite T. Compared to the significant hardening of the scattering rates by T, the weak change in the phonon group velocities, suggesting the effect of anharmonic renormalization on phonon group velocities, is less significant. Thus, we contribute to the underlying physical microscopic mechanisms of weak dependence of κ_p on T with a balance between two features: (i) as T increases, the increased phonon population that obeys the Bose-Einstein statistics generally enhances the scattering rates; and (ii) whereas, phonon anharmonic renormalization induces phonon continuous stiffening and reduces scattering rates in the low-energy region, especially for acoustic- and quasilocalized optical phonon modes associated with the Ag-Ag dimers rattling-like vibrations.

According to PBTE anharmonic theory, the scattering rates depend on both (i) the anharmonic interaction matrix and (ii) the proportional phonon scattering space. To gain a deeper microscopic origin of the reduction of scattering rates due to phonon anharmonic renormalization, we plot the phonon scattering space as a function of frequency. The three-phonon scattering processes are described as combination process ($\lambda^+ : \zeta + \zeta_1 \rightarrow \zeta_2$) and splitting process ($\lambda^- : \zeta \rightarrow \zeta_1 + \zeta_2$). As Fig. 4(d) shows, the combination process dominates the low-energy region, whereas the splitting process prevails in the high-energy region. Taking into account the phonon anharmonic renormalization, both λ^+ and λ^- show a significant reduction in the low-energy region upon heating. Meanwhile, it can be further verified by the decreased anharmonic coupling coefficient in the low-energy regions of LA modes at X point at different T (see Fig. S11 in the SM) [63]. According to anharmonic theory [70], we conclude that multiphonon interaction induces phonon blueshift in the low-energy region, diminishing the strength of the coupling between acoustic and optical modes in the low-energy area and thus decreasing the scatting rates as well. It verifies the reduction of the scattering rates in the low-energy area and $S_{\mathbf{q},s}(\omega)$ of all phonon modes become weaker, broader, and hardener on heating.

Here, we revisit the phonon quasiparticle physical picture. The conventional phonon gas that works well should meet two features: (i) each phonon mode should possess a long enough mean-free path (MFP) to define its wave vector or (ii) each phonon mode should possess a long enough lifetime to define its frequency [20]. In regard to SCP, these anharmonic renormalized phonons are beyond the conventional harmonic

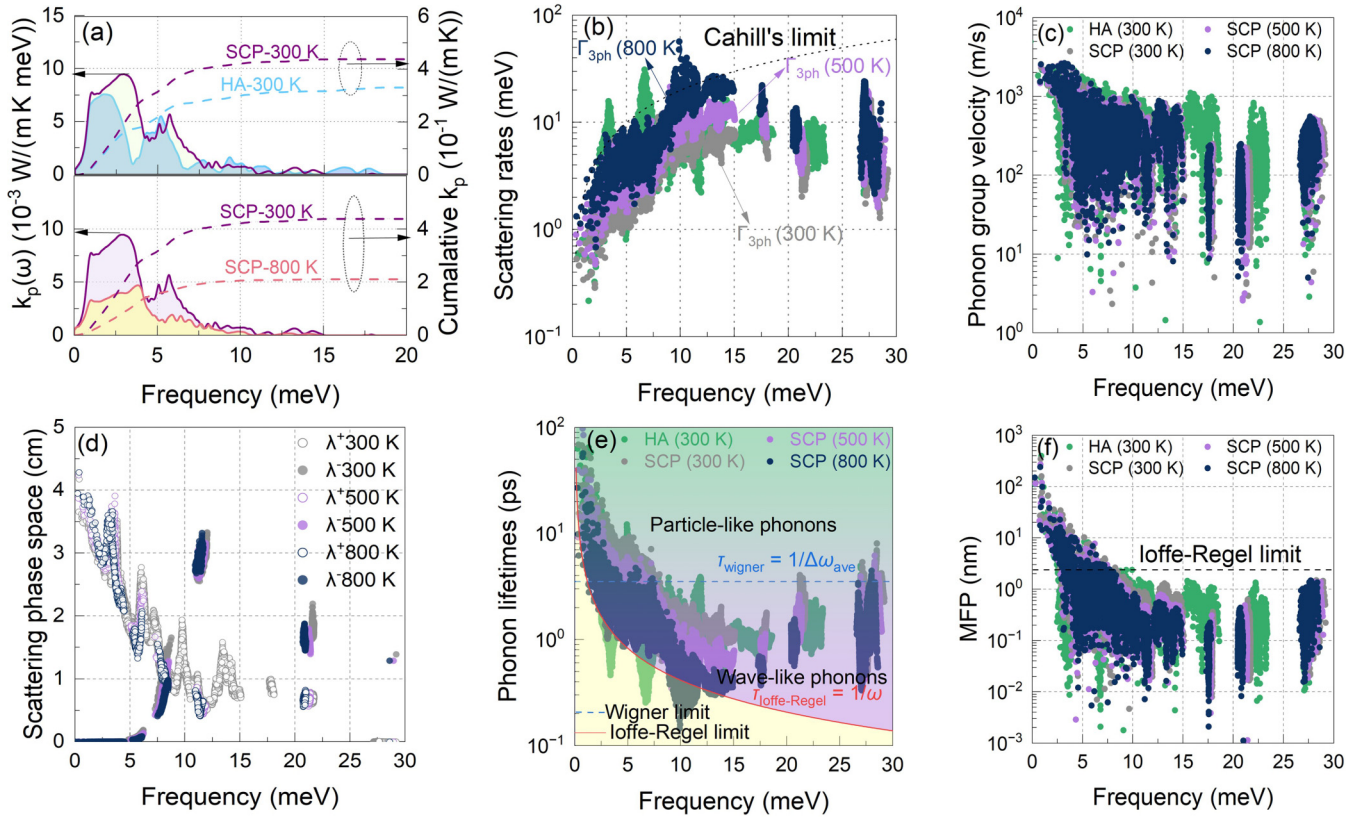

FIG. 4. (a) Comparisons of the spectral and cumulative (dashed lines) κ_L obtained from HA/SCP+PBTE at 300 K (upper panel) and from SCP+PBTE at 300 and 800 K (lower panel). (b) Phonon scattering rates at 300 (gray dots), 500 (purple dots), and 800 K (dark-blue dots) in the frame of SCP+PBTE as well as the results calculated in the frame of HA+PBTE at 300 K (green dots). The black dashed line assumes the scattering rates of phonon modes to be twice their frequencies according to the Cahill-Watson-Pohl model, namely, the Cahill limit or amorphous limit [18]. (c) Phonon group velocities at 300 (gray dots), 500 (purple dots), and 800 K (dark blue dots) from SCP as well as results at 300 K from HA (green dots). (d) Energy- and momentum-conserving three-phonon scattering phase space at finite T, where the hollow and filled dots represent the combination process ($\lambda^+ : \zeta + \zeta_1 \rightarrow \zeta_2$) and the splitting process ($\lambda- : \zeta \rightarrow \zeta_1 + \zeta_2$), respectively [68]. (e) Phonon relaxation time τ at finite T. The Ioffe-Regel limit (τ equals the inverse of the phonon frequency, i.e., $\tau_{\text{Ioffe-Regel}} = 1/\omega$) [20] and the Wigner limit (τ equals the inverse of the average interband spacing, i.e., $\tau_{\text{Wigner}} = 1/\Delta\omega_{\text{ave}} = 3\text{Nat}/\omega_{\max}$, where N_{at} is the number of atoms and $\omega_{\max}$ is the maximum frequency) [25] are also indicated. (f) Mean-free path (MFP) as a function of frequencies at finite T, where the Ioffe-Regel limit represent the smallest atomic distance.

approximation but are quasiparticle excitations corresponding to the poles of Green's function [34,64]. These phonons preserve well-defined frequency, linewidths, and eigenvectors and can form propagating wave packets. To understand the discrepancy between κ_p^{avg} and κ_L^{avg}, we further plot phonon mode lifetimes and MFPs as a function of frequency at finite T. In Fig. 4(e), we explain it by showing along with τ, the Wigner limit τ_{Wigner}. and the Ioffe-Regel limit $\tau_{\text{Ioffe-Regel}}$. Phonons with $\tau > \tau_{\text{Wigner}}$ behave as particle-like phonons that contribute mainly to κ_p, whereas the large phonons population with $\tau_{\text{Ioffe-Regel}} < \tau < \tau_{\text{Wigner}}$ displays wavelike phonons feature that contributes mainly to κ_c [25]. Meanwhile, generous phonons exist below the Ioffe-Regel limit and thus contribute evidently to the wavelike phonon tunneling thermal transport [see Fig. 4(f)]. Numerous phonons behave as wavelike thermal carriers and lead to the noneligible κ_c, suggesting the qualitative breakdown of the conventional phonon gas model [21].

To obtain a deeper understanding of the microscopic mechanisms of the wavelike phonon tunneling thermal transport, we plot three-dimensional visualizations of the mode-specific contribution to κ_c as a function of anharmonically renormalized phonon frequencies at $T = 300$ K for κ_c^{abc}. Results show that the phonons below 10 meV exhibit very tiny discrepancy frequencies, i.e., quasidegenrate vibration eigenstates dominate the wavelike phonons tunneling thermal transport. The diagonal area contributes most to the coherent thermal conductivity because of the localization of the phonon energy power spectral. See Fig. 5.

Besides, the anisotropy ratio of κ_p is much stronger than that of κ_c, e.g., $\kappa_p^a/\kappa_p^b/\kappa_p^c = 2.40/1/1.60$ and $\kappa_c^a/\kappa_c^b/\kappa_c^c = 1.17/1/1.15$ at 300 K. The anisotropy in κ p can be ascribed to the special tunnel structure of $BaAg_2SnSe_4$ as we mentioned above. According to previous studies [65], low κ_p generally means large phonon linewidth. It usually results in larger κ_c due to strong coherent coupling between different vibration eigenstates. However, in the case of quaternary compound $BaAg_2SnSe_4$, this phenomenon does not display, which is puzzling. To reveal the microscopic origin of such unusual

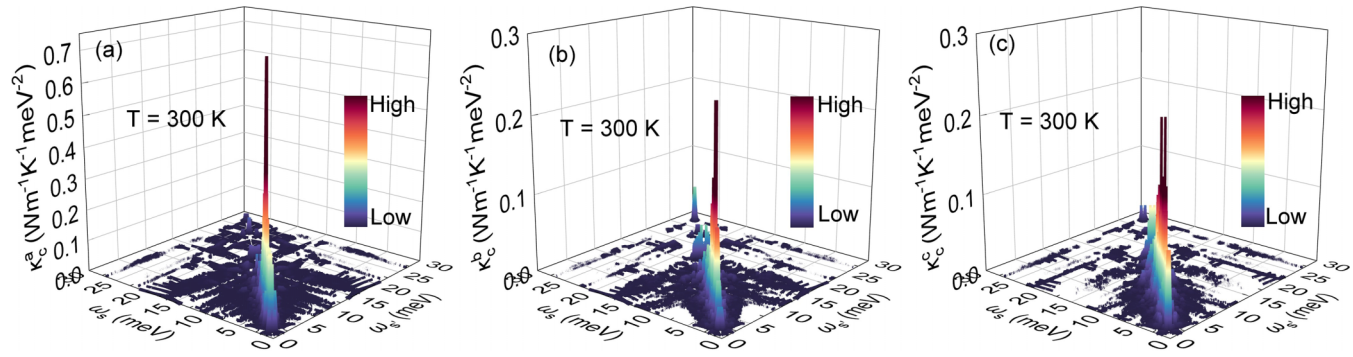

FIG. 5. Three-dimensional visualizations of the mode-specific contributions to the wavelike phonons' tunneling thermal transport channel at $T = 300$ K. (a)–(c) denote the results along the three Cartesian directions a, b, and c, respectively. A color scale corresponding to the variation of colors in each plot is shown and it has the same unit as indicated in the z axis.

thermal transport behavior, we note that the coherent thermal conductivity takes place between coupled phonon eigenstates through the generalized phonon group velocities operator. Our results indicate that the diagonal term of the generalized phonon group velocities operator follows the order $V_x > V_z > V_y$ (see Fig. S12 in the SM) [63]. This relation is also applicable to describe the nondiagonal term which contributes to the coherent thermal conductivity. Thus, this unusual thermal transport behavior can be attributed to the competition between the nondiagonal term of the generalized phonon group velocities operator and the phonon interbranch broadening coupling [20]. However, the nondiagonal term of the phonon group velocity has a weak dependence on the slopes of the phonon branches, which partially counteracts the anisotropy in κ_p. In this regard, the modulation of phonon group velocity can effectively tailor κ_L, which includes both the particle-like propagation of phonon wave packets and the wavelike phonon tunneling of heat carrying.

E. Discussion

In quaternary compound $BaAg_2SnSe_4$, the Ag atoms' rattling-like vibrations, the quasilocalized optical phonon modes, and the dense low-frequency phonon branches are intimately related to each other and are the origin of the weak T dependence of the ultralow κ_L. In Fig. 6, we compare the experimental results of κ_L of $BaAg_2SnSe_4$ with

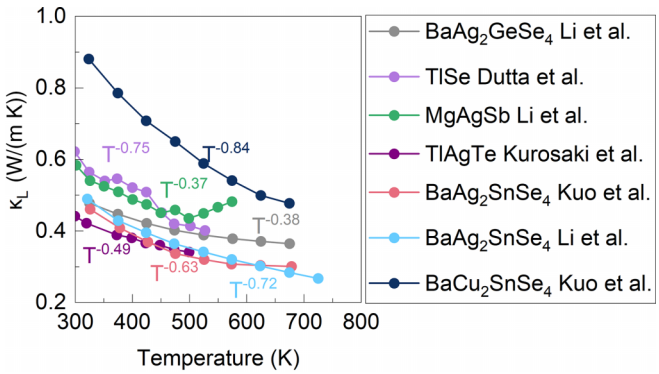

FIG. 6. Comparison with various experimental measured κ_L values of various copper-based or silver-based thermoelectric materials [6,49–51,79,80]. The κ_L dependences on T of them are also marked.

experimental data of other related copper-based or silver-based thermoelectric materials [6,49–51,79,80]. As shown, the weak T dependence of κ_L is universal in many copper (silver)-based thermoelectric materials or strong anharmonic systems. Phonon anharmonic hardening effect and two-channel thermal transport model can broadly explain the weak T dependence of severely anharmonic materials. However, for some superionic conductors, Cu/Ag ions can move randomly in the lattice and deviate sharply from the equilibrium position behavior as liquid, rendering anharmonic theory no longer applicable, e.g., Cu_2Se [45].

Besides, our present results indicate a slight deviation of the calculated κ_L from the experimental value. However, this discrepancy is acceptable. We perform a comprehensive analysis for limitations of the theory model: (i) RTA [32], (ii) thermal expansion effect, (iii) anharmonic contribution of heat-flux operator [81], and (iv) four-phonon scattering rates. Feature (i) incorrectly considers normal phonon-phonon processes as resistive, which could modestly underestimate the thermal conductivity for low κ_L. Feature (ii) generally softens phonon frequencies, widens the phonon energy power spectral, and thus decreases κ_L. However, the phonon softening effect on κ_L of feature (ii) can be partially counterbalanced by feature (iii) [21,81]. Wigner thermal transport is derived from the harmonic heat-flux operator and thus does not contain the information of anharmonic heat flux [22,25,81]. Feature (iv) could give more accurate phonon linewidths in principle; however, the calculations are computationally extremely expensive for noncubic lattice with a dense q-mesh grid [82–85]. On the other hand, those non-Lorentzian line shapes' phonon modes' lifetime can be further expressed as a more generalized Green-Kubo formula [86,87].

IV. CONCLUSIONS

In conclusion, we have investigated the anharmonic lattice dynamics and thermal transport property in $BaAg_2SnSe_4$ based on the top of SCP theory which considers both bubble and loop diagrams. Within the Wigner thermal transport model, we take into account the phonon anharmonic renormalization and the wavelike phonon tunneling thermal transport channel. The phonon energy power spectral of the low-frequency phonon modes becomes weaker, broader, and hardener as T increases, suggesting the anharmonic hardening

effect induced by the quartic anharmonicity. This anharmonic hardening behavior is mainly associated with the disorder Ag-Ag dimers' rattling-like vibrations, suppressing the scattering strength of the low-frequency phonon modes via decreasing scattering phase space, partially counteracting the increasing phonon population, and thereby yielding a slow reduction of κ_L. Furthermore, both the particle-like phonon propagates wave packets and the wavelike phonon tunneling thermal transport channel must be considered to capture and reproduce the experimentally measured values of κ_L both in magnitude and T dependence. The low κ_L as well as its anomalous T-dependent behaviors can be attributed to the fact that strong phonon broadening induces coherent coupling between different vibrational eigenstates, resulting in the partial breakdown of the conventional phonon gas model. A non-negligible compensation of the κ_L by the off-diagonal term of the heat-flow operators is indispensable, especially under high T. This work demonstrates the importance of phonon anharmonic renormalization and wavelike phonon tunneling thermal transport channel in anharmonic lattice dynamics and thermal transport of severely anharmonic materials.

ACKNOWLEDGMENTS

The authors gratefully acknowledge financial support from the National Natural Science Foundation of China (Grants No. 12074381 and No. U2330104). The calculations were performed at CSNS Scientific Computing Platform of Institute of High Energy Physics of CAS and GBA Sub-center of National HEP Science Data Center.

[1] L. E. Bell, Cooling, heating, generating power, and recovering waste heat with thermoelectric systems, Science **321**, 1457 (2008).

[2] G. J. Snyder and E. S. Toberer, Complex thermoelectric materials, Nat. Mater. **7**, 105 (2008).

[3] H. J. Wu, L. D. Zhao, F. S. Zheng, D. Wu, Y. L. Pei, X. Tong, M. G. Kanatzidis, and J. Q. He, Broad temperature plateau for thermoelectric figure of merit ZT > 2 in phase-separated $PbTe_{0.7}S_{0.3}$, Nat. Commun. **5**, 4515 (2014).

[4] M. Christensen, A. B. Abrahamsen, N. B. Christensen, F. Juranyi, N. H. Andersen, K. Lefmann, J. Andreasson, C. R. H. Bahl, and B. B. Iversen, Avoided crossing of rattler modes in thermoelectric materials, Nat. Mater. **7**, 811 (2008).

[5] P.-F. Liu, X. Li, J. Li, J. Zhu, Z. Tong, M. Kofu, M. Nirei, J. Xu, W. Yin, F. Wang, T. Liang, L. Xie, Y. Zhang, D. J. Singh, J. Ma, H. Lin, J. Zhang, J. He, and B.-T. Wang, Strong low-energy rattling modes enabled liquid-like ultralow thermal conductivity in a well-ordered solid, Natl. Sci. Rev. nwae216 (2024).

[6] X. Li, P.-F. Liu, E. Zhao, Z. Zhang, T. Guidi, M. D. Le, M. Avdeev, K. Ikeda, T. Otomo, M. Kofu, K. Nakajima, J. Chen, L. He, Y. Ren, X.-L. Wang, B.-T. Wang, Z. Ren, H. Zhao, and F. Wang, Ultralow thermal conductivity from transverse acoustic phonon suppression in distorted crystalline α-MgAgSb, Nat. Commun. **11**, 942 (2020).

[7] K. Pal, J. He, and C. Wolverton, Bonding hierarchy gives rise to high thermoelectric performance in layered Zintl compound $BaAu_2P_4$, Chem. Mater. **30**, 7760 (2018).

[8] Y. Zhou and L.-D. Zhao, Promising thermoelectric bulk materials with 2D structures, Adv. Mater. **29**, 1702676 (2017).

[9] J. R. Tillman, Progress in semiconductors, Nature (London) **178**, 508 (1956).

[10] Y. Luo, X. Yang, T. Feng, J. Wang, and X. Ruan, Vibrational hierarchy leads to dual-phonon transport in low thermal conductivity crystals, Nat. Commun. **11**, 2554 (2020).

[11] X. Chen, A. Weathers, J. Carrete, S. Mukhopadhyay, O. Delaire, D. A. Stewart, N. Mingo, S. N. Girard, J. Ma, D. L. Abernathy, J. Yan, R. Sheshka, D. P. Sellan, F. Meng, S. Jin, J. Zhou, and L. Shi, Twisting phonons in complex crystals with quasi-one-dimensional substructures, Nat. Commun. **6**, 6723 (2015).

[12] M. T. Agne, R. Hanus, and G. J. Snyder, Minimum thermal conductivity in the context of diffuson-mediated thermal transport, Energ Environ. Sci. **11**, 609 (2018).

[13] S. Mukhopadhyay, D. S. Parker, B. C. Sales, A. A. Puretzky, M. A. McGuire, and L. Lindsay, Two-channel model for ultralow thermal conductivity of crystalline Tl_3VSe_4, Science **360**, 1455 (2018).

[14] A. Einstein, Elementare Betrachtungen über die thermische Molekularbewegung in festen Körpern, Ann. Phys. **340**, 679 (1911).

[15] W. Lv and A. Henry, Non-negligible contributions to thermal conductivity from localized modes in amorphous silicon dioxide, Sci. Rep. **6**, 35720 (2016).

[16] J. L. Cohn, G. S. Nolas, V. Fessatidis, T. H. Metcalf, and G. A. Slack, Glasslike heat conduction in high-mobility crystalline semiconductors, Phys. Rev. Lett. **82**, 779 (1999).

[17] D. T. Morelli and G. P. Meisner, Low temperature properties of the filled skutterudite $CeFe_4Sb_{12}$, J. Appl. Phys. **77**, 3777 (1995).

[18] D. G. Cahill, S. K. Watson, and R. O. Pohl, Lower limit to the thermal conductivity of disordered crystals, Phys. Rev. B **46**, 6131 (1992).

[19] P. B. Allen and J. L. Feldman, Thermal conductivity of glasses: Theory and application to amorphous Si, Phys. Rev. Lett. **62**, 645 (1989).

[20] P. B. Allen and J. L. Feldman, Thermal conductivity of disordered harmonic solids, Phys. Rev. B **48**, 12581 (1993).

[21] T. Sun and P. B. Allen, Lattice thermal conductivity: Computations and theory of the high-temperature breakdown of the phonon-gas model, Phys. Rev. B **82**, 224305 (2010).

[22] M. Simoncelli, N. Marzari, and F. Mauri, Unified theory of thermal transport in crystals and glasses, Nat. Phys. **15**, 809 (2019).

[23] Y. Xia, K. Pal, J. He, V. Ozoliņš, and C. Wolverton, Particlelike phonon propagation dominates ultralow lattice thermal conductivity in crystalline Tl_3VSe_4, Phys. Rev. Lett **124**, 065901 (2020).

[24] Y. Xia, V. Ozoliņš, and C. Wolverton, Microscopic mechanisms of glasslike lattice thermal transport in cubic $Cu_{12}Sb_4S_{13}$ tetrahedrites, Phys. Rev. Lett. **125**, 085901 (2020).

[25] M. Simoncelli, N. Marzari, and F. Mauri, Wigner formulation of thermal transport in solids, Phys. Rev. X **12**, 041011 (2022).

[26] X. Yang, T. Feng, J. S. Kang, Y. Hu, J. Li, and X. Ruan, Observation of strong higher-order lattice anharmonicity in Raman and infrared spectra, Phys. Rev. B **101**, 161202(R) (2020).

[27] A. Debernardi, S. Baroni, and E. Molinari, Anharmonic phonon lifetimes in semiconductors from density-functional perturbation theory, Phys. Rev. Lett **75**, 1819 (1995).

[28] B. Yang and G. Chen, Partially coherent phonon heat conduction in superlattices, Phys. Rev. B **67**, 195311 (2003).

[29] E. Dechaumphai and R. Chen, Thermal transport in phononic crystals: The role of zone folding effect, J. Appl. Phys. **111**, 073508 (2012).

[30] X. He, D. Bansal, B. Winn, S. Chi, L. Boatner, and O. Delaire, Anharmonic eigenvectors and acoustic phonon disappearance in quantum paraelectric $SrTiO_3$, Phys. Rev. Lett **124**, 145901 (2020).

[31] T. Tadano, Y. Gohda, and S. Tsuneyuki, Anharmonic force constants extracted from first-principles molecular dynamics: Applications to heat transfer simulations, J. Phys.: Condens. Matter **26**, 225402 (2014).

[32] T. Tadano, Y. Gohda, and S. Tsuneyuki, Impact of rattlers on thermal conductivity of a thermoelectric clathrate: A first-principles study, Phys. Rev. Lett. **114**, 095501 (2015).

[33] T. Tadano and S. Tsuneyuki, Quartic anharmonicity of rattlers and its effect on lattice thermal conductivity of clathrates from first principles, Phys. Rev. Lett. **120**, 105901 (2018).

[34] T. Tadano and W. A. Saidi, First-principles phonon quasiparticle theory applied to a strongly anharmonic halide perovskite, Phys. Rev. Lett. **129**, 185901 (2022).

[35] F. Zhou, W. Nielson, Y. Xia, and V. Ozoliņš, Lattice anharmonicity and thermal conductivity from compressive sensing of first-principles calculations, Phys. Rev. Lett. **113**, 185501 (2014).

[36] M. Dutta, K. Pal, U. V. Waghmare, and K. Biswas, Bonding heterogeneity and lone pair induced anharmonicity resulted in ultralow thermal conductivity and promising thermoelectric properties in n-type $AgPbBiSe_3$, Chem. Sci. **10**, 4905 (2019).

[37] K. Majhi, K. Pal, H. Lohani, A. Banerjee, P. Mishra, A. K. Yadav, R. Ganesan, B. R. Sekhar, U. V. Waghmare, and P. S. Anil Kumar, Emergence of a weak topological insulator from the Bi_xSe_y family, Appl. Phys. Lett. **110**, 162102 (2017).

[38] W. Qiu, L. Xi, P. Wei, X. Ke, J. Yang, and W. Zhang, Part-crystalline part-liquid state and rattling-like thermal damping in materials with chemical-bond hierarchy, Proc. Natl. Acad. Sci. USA **111**, 15031 (2014).

[39] C. Wang, Y. Wu, Y. Pei, and Y. Chen, Dynamic disorder phonon scattering mediated by Cu atomic hopping and diffusion in Cu_3SbSe_3, Npj Comput. Mater. **6**, 155 (2020).

[40] L. Xie, J. H. Feng, R. Li, and J. Q. He, First-principles study of anharmonic lattice dynamics in low thermal conductivity $AgCrSe_2$: Evidence for a large resonant four-phonon scattering, Phys. Rev. Lett. **125**, 245901 (2020).

[41] J. Ding, J. L. Niedziela, D. Bansal, J. Wang, X. He, A. F. May, G. Ehlers, D. L. Abernathy, A. Said, A. Alatas, Y. Ren, G. Arya, and O. Delaire, Anharmonic lattice dynamics and superionic transition in $AgCrSe_2$, Proc. Natl. Acad. Sci. **117**, 3930 (2020).

[42] C. Wang and Y. Chen, Highly selective phonon diffusive scattering in superionic layered $AgCrSe_2$, npj Comput. Mater. **6**, 26 (2020).

[43] B. Li, H. Wang, Y. Kawakita, Q. Zhang, M. Feygenson, H. L. Yu, D. Wu, K. Ohara, T. Kikuchi, K. Shibata, T. Yamada, X. K. Ning, Y. Chen, J. Q. He, D. Vaknin, R. Q. Wu, K. Nakajima, and M. G. Kanatzidis, Liquid-like thermal conduction in intercalated layered crystalline solids, Nat. Mater. **17**, 226 (2018).

[44] K. Zhao, A. B. Blichfeld, H. Chen, Q. Song, T. Zhang, C. Zhu, D. Ren, R. Hanus, P. Qiu, B. B. Iversen, F. Xu, G. J. Snyder, X. Shi, and L. Chen, Enhanced thermoelectric performance through tuning bonding energy in $Cu_2Se_{1-x}S_x$ liquid-like materials, Chem. Mater. **29**, 6367 (2017).

[45] H. Liu, X. Shi, F. Xu, L. Zhang, W. Zhang, L. Chen, Q. Li, C. Uher, T. Day, and G. J. Snyder, Copper ion liquid-like thermoelectrics, Nat. Mater. **11**, 422 (2012).

[46] H. Lin, G. Tan, J.-N. Shen, S. Hao, L.-M. Wu, N. Calta, C. Malliakas, S. Wang, C. Uher, C. Wolverton, and M. G. Kanatzidis, Concerted rattling in $CsAg_5Te_3$ leading to ultralow thermal conductivity and high thermoelectric performance, Angew. Chem. Int. Ed. **55**, 11431 (2016).

[47] N. Ma, F. Li, J.-G. Li, X. Liu, D.-B. Zhang, Y.-Y. Li, L. Chen, and L.-M. Wu, Mixed-valence $CsCu_4Se_3$: Large phonon anharmonicity driven by the hierarchy of the rigid $[(Cu^+)_4(Se^{2-})_2](Se^-)$ double Anti-CaF_2 layer and the soft Cs^+ sublattice, J. Am. Chem. Soc. **143**, 18490 (2021).

[48] A. Hong and L. Ma, Ultralow thermal conductivity in quaternary compound $Ag_2BaSnSe_4$ due to square-cylinder cage-like structure with rattling vibration, Appl. Phys. Lett. **118**, 143903 (2021).

[49] Y. Li, Z. Li, C. Zhang, D. Yang, T. Liu, Y. Yan, W. Liu, G. Tan, X. Su, C. Uher, and X. Tang, Ultralow thermal conductivity of $BaAg_2SnSe_4$ and the effect of doping by Ga and In, Mater. Today Phys. **9**, 100098 (2019).

[50] W. D. C. B. Gunatilleke, A. F. May, H. Wang, and G. S. Nolas, Thermal properties of $BaCu_2SnQ_4$ (Q = S, Se) quaternary chalcogenides, Appl. Phys. Lett. **117**, 092101 (2020).

[51] J. J. Kuo, U. Aydemir, J.-H. Pöhls, F. Zhou, G. Yu, A. Faghaninia, F. Ricci, M. A. White, G.-M. Rignanese, G. Hautier, A. Jain, and G. J. Snyder, Origins of ultralow thermal conductivity in 1-2-1-4 quaternary selenides, J. Mater Chem. A **7**, 2589 (2019).

[52] Z. Chang, J. Zheng, J. Ma, X. Zhang, Y. Gao, and D. Tang, Temperature-dependent interatomic force constants and phonon coherent resonance contribution in quaternary non-centrosymmetric chalcogenides $BaAg_2SnSe_4$, Int. J. Heat Mass Transfer **219**, 124863 (2024).

[53] P. Hohenberg and W. Kohn, Inhomogeneous electron gas, Phys. Rev **136**, B864 (1964).

[54] P. E. Blöchl, Projector augmented-wave method, Phys. Rev. B **50**, 17953 (1994).

[55] G. Kresse and J. Furthmüller, Efficient iterative schemes for ab initio total-energy calculations using a plane-wave basis set, Phys. Rev. B **54**, 11169 (1996).

[56] A. Togo and I. Tanaka, First principles phonon calculations in materials science, Scr. Mater **108**, 1 (2015).

[57] F. Zhou, W. Nielson, Y. Xia, and V. Ozoliņš, Compressive sensing lattice dynamics. I. General formalism, Phys. Rev. B **100**, 184308 (2019).

[58] F. Zhou, B. Sadigh, D. Åberg, Y. Xia, and V. Ozoliņš, Compressive sensing lattice dynamics. II. Efficient phonon calculations and long-range interactions, Phys. Rev. B **100**, 184309 (2019).

[59] D. West and S. K. Estreicher, First-principles calculations of vibrational lifetimes and decay channels: Hydrogen-related modes in Si, Phys. Rev. Lett. **96**, 115504 (2006).
[60] F. Eriksson, E. Fransson, and P. Erhart, The hiphive package for the extraction of high-order force constants by machine learning, Adv. Theor. Simul. **2**, 1800184 (2019).
[61] E. J. Candes and M. B. Wakin, An introduction to compressive sampling, IEEE Signal Process Mag. **25**, 21 (2008).
[62] L. J. Nelson, G. L. W. Hart, F. Zhou, and V. Ozoliņš, Compressive sensing as a paradigm for building physics models, Phys. Rev. B **87**, 035125 (2013).
[63] See Supplemental Material at http://link.aps.org/supplemental/10.1103/PhysRevB.110.045203 for information about CSLD fitting error; harmonic and anharmonic force constants versus interaction distance; convergence tests of the calculated κ_p at 300 K with different level method; workflows; element-resolved phonon density of states at finite T; the calculated T-dependent equivalent isotropic displacement parameter; the calculated T-dependent acoustic phonon mode at X point; phonon dispersion curves at different theoretical level; the calculated κ_L without bubble diagram; three-phonon interaction dynamic matrix of the LA mode at X point at finite T; and the calculated anisotropic phonon group velocity, which include Refs. [49,51].
[64] T. Tadano and S. Tsuneyuki, Self-consistent phonon calculations of lattice dynamical properties in cubic $SrTiO_3$ with first-principles anharmonic force constants, Phys. Rev. B **92**, 054301 (2015).
[65] Q.-Y. Xie, P.-F. Liu, J.-J. Ma, L.-M. Wu, K.-W. Zhang, and B.-T. Wang, Microscopic mechanisms of glasslike lattice thermal conductivity in tetragonal α-$CsCu_5Se_3$, Phys. Rev. B **108**, 014302 (2023).
[66] Y. Wang, Q. Gan, M. Hu, J. Li, L. Xie, and J. He, Anharmonic lattice dynamics and the origin of intrinsic ultralow thermal conductivity in AgI materials, Phys. Rev. B **107**, 064308 (2023).
[67] A. Togo, L. Chaput, and I. Tanaka, Distributions of phonon lifetimes in Brillouin zones, Phys. Rev. B **91**, 094306 (2015).
[68] W. Li, J. Carrete, N. A. Katcho, and N. Mingo, ShengBTE: A solver of the Boltzmann transport equation for phonons, Comput. Phys. Commun. **185**, 1747 (2014).
[69] W. Li and N. Mingo, Thermal conductivity of fully filled skutterudites: Role of the filler, Phys. Rev. B **89**, 184304 (2014).
[70] P. G. Klemens, Anharmonic decay of optical phonons, Phys. Rev. **148**, 845 (1966).
[71] S. Karak, J. Bera, S. Paul, S. Sahu, and S. Saha, Low thermal conductivity and interface thermal conductance in SnS_2, Phys. Rev. B **104**, 195304 (2021).
[72] U. Aseginolaza, R. Bianco, L. Monacelli, L. Paulatto, M. Calandra, F. Mauri, A. Bergara, and I. Errea, Phonon collapse and second-order phase transition in thermoelectric SnSe, Phys. Rev. Lett. **122**, 075901 (2019).
[73] C. W. Li, O. Hellman, J. Ma, A. F. May, H. B. Cao, X. Chen, A. D. Christianson, G. Ehlers, D. J. Singh, B. C. Sales, and O. Delaire, Phonon self-energy and origin of anomalous neutron scattering spectra in SnTe and PbTe thermoelectrics, Phys. Rev. Lett. **112**, 175501 (2014).
[74] R. Bianco, I. Errea, M. Calandra, and F. Mauri, High-pressure phase diagram of hydrogen and deuterium sulfides from first principles: Structural and vibrational properties including quantum and anharmonic effects, Phys. Rev. B **97**, 214101 (2018).
[75] O. Delaire, J. Ma, K. Marty, A. F. May, M. A. McGuire, M. H. Du, D. J. Singh, A. Podlesnyak, G. Ehlers, M. D. Lumsden, and B. C. Sales, Giant anharmonic phonon scattering in PbTe, Nat. Mater. **10**, 614 (2011).
[76] L. Paulatto, I. Errea, M. Calandra, and F. Mauri, First-principles calculations of phonon frequencies, lifetimes, and spectral functions from weak to strong anharmonicity: The example of palladium hydrides, Phys. Rev. B **91**, 054304 (2015).
[77] S. Mukhopadhyay, D. Bansal, O. Delaire, D. Perrodin, E. Bourret-Courchesne, D. J. Singh, and L. Lindsay, The curious case of cuprous chloride: Giant thermal resistance and anharmonic quasiparticle spectra driven by dispersion nesting, Phys. Rev. B **96**, 100301(R) (2017).
[78] B. Hennion, B. Prevot, M. Krauzman, R. M. Pick, and B. Dorner, Neutron scattering of the TO phonon in CuCl at 5 K, J. Phys. C; Solid State Phys. **12**, 1609 (1979).
[79] M. Dutta, S. Matteppanavar, M. V. D. Prasad, J. Pandey, A. Warankar, P. Mandal, A. Soni, U. V. Waghmare, and K. Biswas, Ultralow thermal conductivity in chain-like TlSe due to inherent Tl^+ rattling, J. Am. Chem. Soc **141**, 20293 (2019).
[80] K. Kurosaki, K. Goto, H. Muta, and S. Yamanaka, Enhancement of thermoelectric figure of merit of AgTlTe by tuning the carrier concentration, J. Appl. Phys **102**, 023707 (2007).
[81] R. J. Hardy, Energy-flux operator for a lattice, Phys. Rev. **132**, 168 (1963).
[82] N. K. Ravichandran and D. Broido, Phonon-phonon interactions in strongly bonded solids: Selection rules and higher-order processes, Phys. Rev. X **10**, 021063 (2020).
[83] Z. Han, X. Yang, W. Li, T. Feng, and X. Ruan, FourPhonon: An extension module to ShengBTE for computing four-phonon scattering rates and thermal conductivity, Comput. Phys. Commun. **270**, 108179 (2022).
[84] T. Feng and X. Ruan, Quantum mechanical prediction of four-phonon scattering rates and reduced thermal conductivity of solids, Phys. Rev. B **93**, 045202 (2016).
[85] T. Feng, L. Lindsay, and X. Ruan, Four-phonon scattering significantly reduces intrinsic thermal conductivity of solids, Phys. Rev. B **96**, 161201(R) (2017).
[86] Đ. Dangić, O. Hellman, S. Fahy, and I. Savić, The origin of the lattice thermal conductivity enhancement at the ferroelectric phase transition in GeTe, npj Comput. Mater. **7**, 57 (2021).
[87] G. Caldarelli, M. Simoncelli, N. Marzari, F. Mauri, and L. Benfatto, Many-body Green's function approach to lattice thermal transport, Phys. Rev. B **106**, 024312 (2022).